

A metal-free photoactive nitrogen-doped carbon nanosolenoid with broad absorption in visible region for efficient photocatalysis

Received: 21 April 2023

Accepted: 4 September 2023

Published online: 20 September 2023

Check for updates

Yu Zhou^{1,2,5}, Xinyu Zhang^{2,5}, Guan Sheng^{3,5}, Shengda Wang², Muqing Chen¹✉, Guilin Zhuang⁴, Yihan Zhu³✉ & Pingwu Du²✉

Riemann surfaces inspired chemists to design and synthesize such multi-dimensional curved carbon architectures. It has been predicted that carbon nanosolenoid materials with Riemann surfaces have unique structures and novel physical properties. Here we report the first synthesis of a nitrogen-doped carbon nanosolenoid (**N-CNS**) using bottom-up approach with a well-defined structure. **N-CNS** was obtained by a rational Suzuki polymerization, followed by oxidative cyclodehydrogenation. The successful synthesis of **N-CNS** was fully characterized by GPC, FTIR, solid-state ¹³C NMR and Raman techniques. The intrinsic single-strand molecular structures of **N-CNS** helices can be clearly resolved using low-dose integrated differential phase contrast scanning transmission electron microscopy (iDPC-STEM) technique. Possessing unique structural and physical properties, this long π -extended polymer **N-CNS** can provide new insight towards bottom-up syntheses of curved nanoribbons and potential applications as a metal-free photocatalyst for visible-light-driven H₂ evolution and highly efficient photocatalyst for photo-redox organic transformations.

In recent years, syntheses of nonplanar polycyclic aromatic hydrocarbons (PAHs) have attracted increasing attention due to their unique structures and novel physical properties^{1–5}. Nonplanar carbon-based π -conjugated systems can be constructed with different topologies of bowls, hoops, and saddles, which can be considered as conjugated segments of larger OD to 3D systems such as fullerenes^{6–9}, carbon nanotubes^{10,11}, helical nanocarbons^{12–15}, and porous graphene sheets^{16,17}. Riemann surfaces are curved helical structures in chemistry, described as deformed versions of the complex plane in mathematics. Carbon nanosolenoids can be considered to follow a Riemann surface¹⁸, in which one atomic carbon layer continuously spirals

around the line perpendicular to the basal plane. Interestingly, Riemann surfaces were proposed as well-known objects in complex analysis and inspired scientists to design multidimensional carbon architectures (Fig. 1a)¹⁹. Some nonplanar structures were predicted to have many interesting mechanical, electronic, and magnetic properties^{20,21}.

Narrow strips of graphene with abundant edges and high aspect ratios, called graphene nanoribbons (GNRs), have great potential applications in photonics, electronics, and energy science^{22–24}. Using a top-down method, GNRs can be synthesized by breaking apart graphene or carbon nanotubes. However, it is difficult to atomically

¹School of Materials Science and Engineering, Dongguan University of Technology, 523808 Dongguan, Guangdong Province, China. ²Key Laboratory of Precision and Intelligent Chemistry, Anhui Laboratory of Advanced Photon Science and Technology, Department of Materials Science and Engineering, University of Science and Technology of China, 96 Jinzhai Road, 230026 Hefei, Anhui Province, China. ³Center for Electron Microscopy, Institute for Frontier and Interdisciplinary Sciences, State Key Laboratory Breeding Base of Green Chemistry Synthesis Technology, College of Chemical Engineering, Zhejiang University of Technology, 18 Chaowang Road, 310014 Hangzhou, Zhejiang Province, China. ⁴College of Chemical Engineering, Zhejiang University of Technology, 18 Chaowang Road, 310014 Hangzhou, Zhejiang Province, China. ⁵These authors contributed equally: Yu Zhou, Xinyu Zhang, Guan Shen.

✉ e-mail: mqchen@ustc.edu.cn; yihanzhu@zjut.edu.cn; dupingwu@ustc.edu.cn

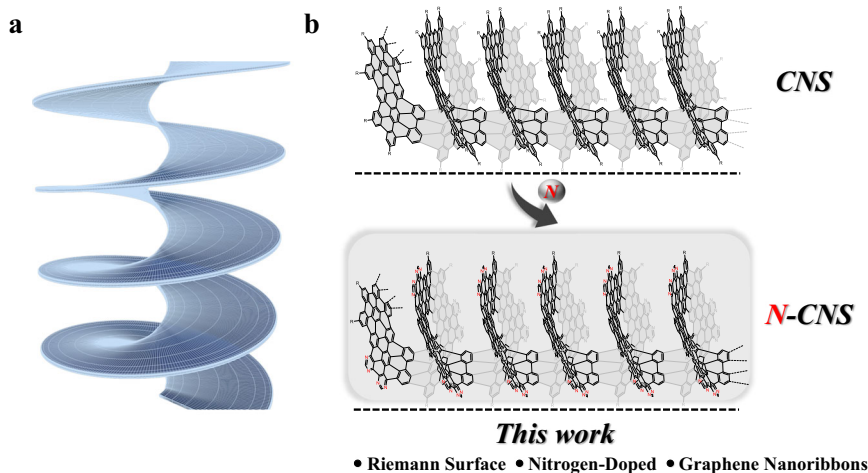


Fig. 1 | Schematic illustrations of Riemann surface and nitrogen-doped carbon nanosolenoids (N-CNS). **a** An example of Riemann's surface. **b** Design of fully π -extended N-CNS.

precise control over the GNR structure and further investigate their applications. Therefore, bottom-up synthesis seems to be a feasible approach to solve this problem. Well-defined GNRs can be constructed by surface-assisted or solution-based polymerization of precursors followed by cyclodehydrogenation reactions^{25–27}. Among them, donor–acceptor (D–A) heterostructures can be fabricated through heteroatom doping in graphene strips with nitrogen, sulfur, and boron atoms at edges^{28–31}. Owing to its electron-donating character and tendency to induce robust ferromagnetism in graphene at a high doping concentration, nitrogen has become the major heteroatom for the synthesis of heterostructures^{32,33}. The electronic properties of GNRs could also be tuned by doping with nitrogen, which has been studied both theoretically and experimentally^{34,35}. Fasel, Müllen, and coworkers used a stepwise cyclization/dehydrogenation sequence on a metal Au(III) surface to obtain nitrogen-doped graphene nanoribbons (N-GNRs), demonstrating a p–n junction character with an electric field of $2 \times 10^8 \text{ V m}^{-1}$ and a band shift of 0.5 eV at the heterojunction³⁶. Moreover, the synthesis of porous N-GNRs was reported by the Meyer group via Ullmann coupling on an Ag(III) surface³⁷. However, surface-assisted synthesis strategies are difficult to scale up and make non-planar 3D strips. Very recently, we developed a facile solution-based strategy to synthesize all-carbon nanosolenoid material with Riemann surface¹⁸. Nanostructured graphitic carbon materials resembling a Riemann surface with helicoid topology are predicted to have interesting magnetic, electrical, and photonic properties^{19–21}. For example, in 2016, Yakobson theoretically predicted a carbon solenoid with Riemann surfaces. This material could emerge a large magnetic field when a voltage is applied and become a brand new magnetic material¹⁹. The following experimental results proved that such carbon nanosolenoid material has magnetic properties¹⁸. Based on these previous results, we speculate that nitrogen-doped carbon nanosolenoid (N-CNS) heterojunction material with Riemann surfaces will possess special optoelectronic and photocatalytic properties, which is unexplored in this field. However, there is no report on the large-scale fabrication of nitrogen-doped carbon nanosolenoid (N-CNS) heterojunction material with Riemann surfaces.

Herein, we report the first synthesis and characterization of such a nitrogen-doped carbon material with interesting physical properties (Fig. 1b). The photophysical properties were investigated using UV–Vis absorption and fluorescence spectroscopy. Furthermore, the broad absorption of N-CNS in the visible region enables it as an excellent special optoelectronic and photocatalytic properties, which is unexplored in this field. However, there is no report on the large-scale fabrication of nitrogen-doped carbon nanosolenoid (N-CNS) heterojunction material with Riemann surfaces.

Herein, we report the first synthesis and characterization of such a nitrogen-doped carbon material with interesting physical properties (Fig. 1b). The photophysical properties were investigated using UV–Vis absorption and fluorescence spectroscopy. Furthermore, the broad absorption of N-CNS in the visible region enables it as an excellent special optoelectronic and photocatalytic properties, which is unexplored in this field. However, there is no report on the large-scale fabrication of nitrogen-doped carbon nanosolenoid (N-CNS) heterojunction material with Riemann surfaces.

environmentally friendly photocatalysts are in high demand for many important energy conversion applications, such as solar water splitting, photocatalytic organic reactions, and so on^{40–42}. In addition, metal-free catalysts are also of great significance in green chemistry and attract much attention in research^{43,44}. Metal-free catalysts have many advantages that include low cost and ready availability, low toxicity, higher stability in air and water, and increased synthetic efficiency due to the avoidance of the time-consuming removal of toxic metal traces. N-CNS, which does not contain any metal component and has photocatalytic properties under visible light, can be used as a potential metal-free catalyst for both visible light-driven H_2 production and efficient photocatalytic organic transformations.

Results

Molecular design of N-CNS

Figure 2 shows the conceptual structure with helicoid topology, in which nanostructured N-doped carbon nanosolenoid material resembles a Riemann surface. The appropriate building units are rationally chosen to obtain the desired structural features. A hexaphenylbenzene (HPB) derivative was chosen as the PAH building unit to achieve the large π -extended feature of N-CNS. To obtain the heterostructure of N-CNS, 5-bromopyrimidine serves as the starting material for introducing nitrogen atoms and Sonogashira coupling can be performed to produce 1,2-di(pyrimidin-5-yl)ethyne. Next, the Diels–Alder reaction between 5,10-dibromo-1,3-diphenyl-2H-cyclopenta[*l*]phenanthren-2-one and 1,2-di(pyrimidin-5-yl)ethyne can afford the HPB derivative unit **M1**. Another building unit **M2** was designed as the linker with two *ortho*-boryl groups to achieve the helicoid topology of N-CNS. Two *ortho-tert*-butyl groups in **M2** were introduced to improve the solubility of precursor **P1** and N-CNS.

Solution synthesis of N-CNS with large lateral π -extension

The synthesis procedure of the N-CNS is summarized in Fig. 2. The essential precursor **P1** was fabricated by combining the molecular building blocks 5,5'-(6,11-dibromo-1,4-diphenyltriphenylene-2,3-diyl)dipyrimidine (**M1**) and 2,2'-(4,4''-di-*tert*-butyl-[1,1':2',1''-terphenyl]-4',5'-diyl)bis(4,4,5,5-tetramethyl-1,3,2-dioxaborolane) (**M2**). Then, **P1** was further performed Scholl reaction to obtain large π -conjugated N-CNS. The detailed synthesis procedure of these molecular building blocks is described in Supplementary Information. The polymerization of **M1** and **M2** was performed by Suzuki–Miyaura coupling reaction using $\text{Pd}(\text{PPh}_3)_4$ as the catalyst, toluene and water as solvents, and reacted at 110 °C for 60 h to obtain the essential precursor (**P1**) with a yield of 83%. Finally, N-CNS was obtained by oxidative

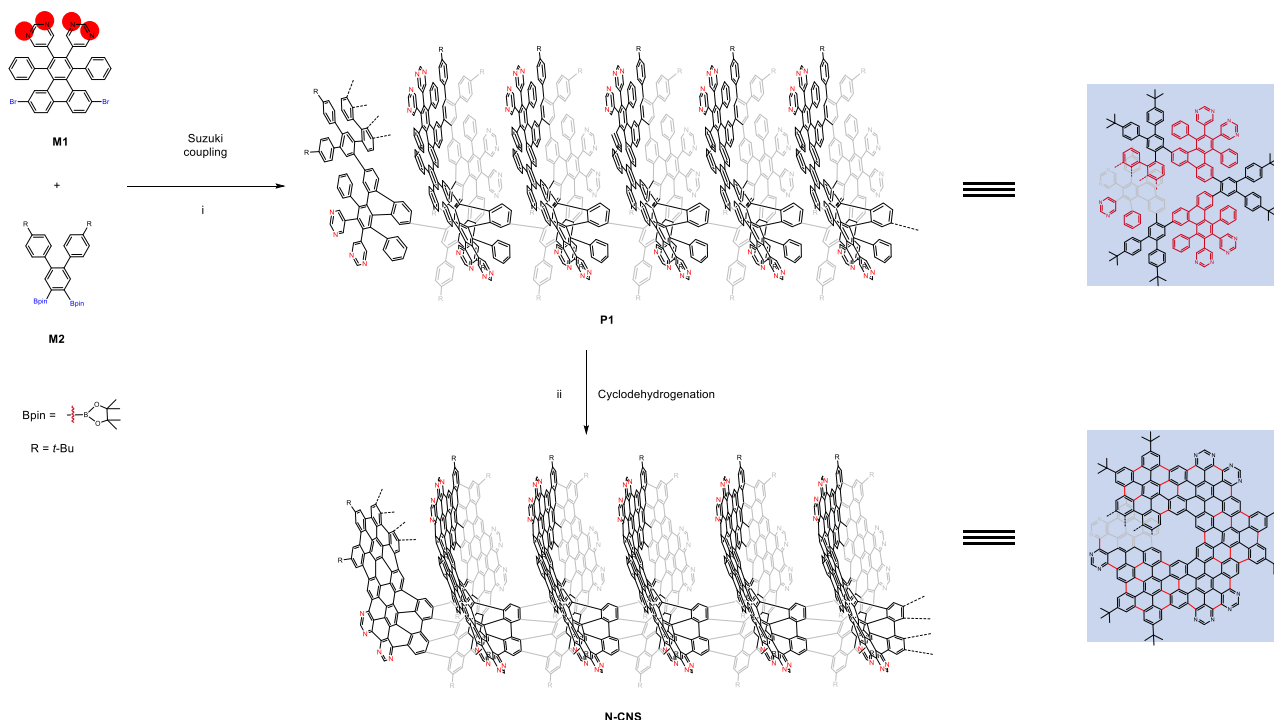


Fig. 2 | Synthetic approach to N-CNS. Reagents and conditions: (i) **M1** (1.0 equiv.), **M2** (1.0 equiv.), K_2CO_3 (10 equiv.), Aliquat 336 (5 mol%), $Pd(PPh_3)_4$ (10 mol%), Ar, toluene/ H_2O (v/v , 5:1), 110 °C, 60 h; (ii) **P1** (1.0 equiv.), DDQ (16 equiv.), TFOH, Ar, anhydrous CH_2Cl_2 , 0 °C, 24 h.

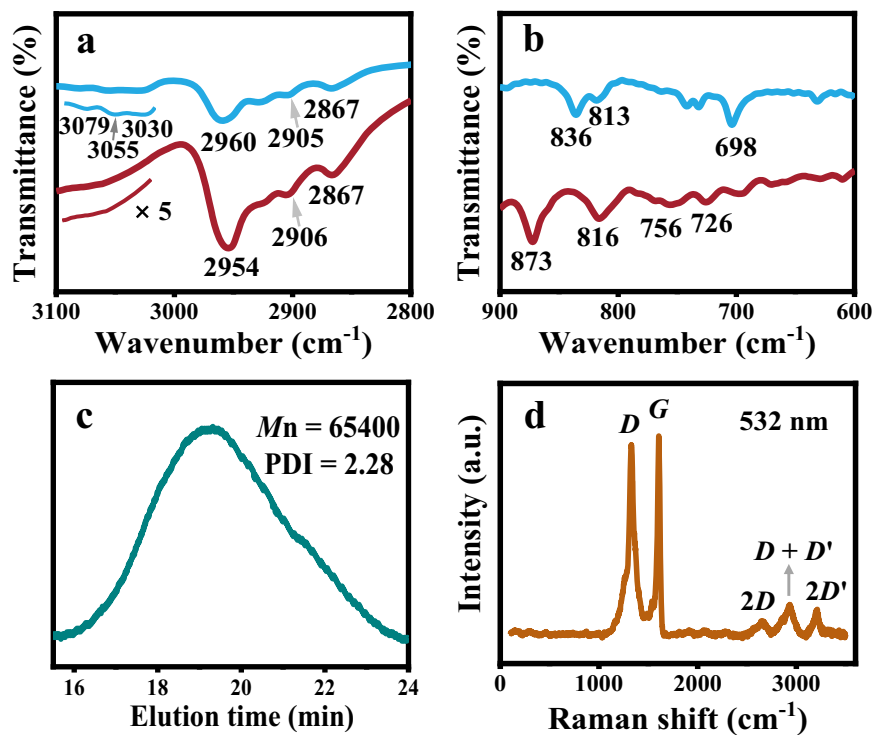


Fig. 3 | Spectroscopic characterization of N-CNS. **a** and **b** Representative FTIR spectral regions of precursor **P1** (blue lines) and **N-CNS** (red lines). **c** GPC trace of **N-CNS**. **d** Raman spectrum of **N-CNS** measured at 532 nm (2.33 eV) on a powder sample.

cyclodehydrogenation of **P1** using 2,3-dichloro-5,6-dicyano-1,4-benzoquinone and trifluoromethanesulfonic acid at 0 °C for 24 h. During the reaction, we found that the solution color quickly turned black, and finally, a dark purple solid was obtained. Moreover, the fluorescence of the solution was changed from blue to red, further

confirming the increasing degree of π -extended conjugation of the backbone.

Gel permeation chromatography (GPC) was used to measure the average molecular weight of **N-CNS** (Fig. 3c). The weight average molecular weight (M_w), relative number-average molecular weight

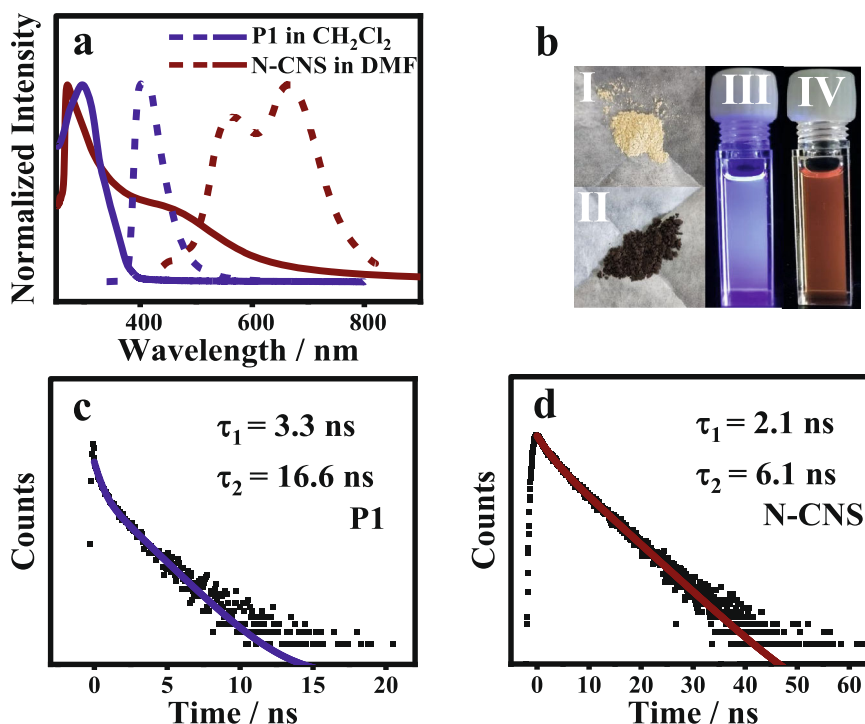


Fig. 4 | Photophysical properties of N-CNS. **a** UV-Vis absorption (dots) and fluorescence spectra (lines) of N-CNS (wine) in DMF and precursor **P1** (blue) in CH_2Cl_2 . **b** Solid powder of precursor **P1** (I) and N-CNS (II), precursor **P1** in CH_2Cl_2

solution (III) and N-CNS in DMF solution (IV) under UV irradiation at 365 nm. **c, d** Emission lifetimes for precursor **P1** in CH_2Cl_2 (black dots: data; blue line: fitting) and N-CNS in DMF (black dots: data; wine line: fitting).

(M_n), and polydispersity index (PDI) of N-CNS were obtained. The molecular weight distribution of N-CNS shows a single broad peak with a PDI of 2.28. The M_n of N-CNS is $65,400 \text{ g mol}^{-1}$. Considering that one helical pitch consists of three monomeric units, this M_n corresponds to ~76 monomer units and contains ~25 spiral pitches.

Bulk spectroscopic characterizations of N-CNS

The highly efficient cyclodehydrogenation of precursor **P1** into N-CNS was confirmed by Fourier transform infrared (FTIR), Raman spectroscopy, and solid-state ^{13}C NMR measurements. FTIR analysis of the material N-CNS after the cyclodehydrogenation revealed that the signals at 3030 , 3055 , and 3079 cm^{-1} originating from aromatic C–H stretching vibrations in **P1** were diminished²⁶. Similar peaks (2906 and 2867 cm^{-1} for N-CNS, 2905 and 2867 cm^{-1} for **P1**) associated with the C–H stretching of alkyl chains were observed upon cyclodehydrogenation, demonstrating the integrity of the alkyl substituents. The vibration bands at 698 , 813 , and 838 cm^{-1} from mono- and disubstituted benzene rings were attenuated (Figs. 3a, b, S2 and S3)⁴⁵. Furthermore, the appearance of a new band maximized at 873 cm^{-1} confirmed the *opla* band which is a typical signal for aromatic C–H at the cove position (Fig. 3b)^{45–47}. All these observations indicate the highly efficient conversion of precursor **P1** into N-CNS.

As a useful tool for characterizing carbon nanomaterials, Raman spectroscopy was performed which is sensitive to the structural and edge defects to confirm the high structural quality of N-CNS. The result shows the typical structural feature for graphene nanoribbons with characteristic intense G and D bands²⁵. The Raman spectrum of N-CNS (excited at 532 nm , powder sample) demonstrates the typical G-band peak and D-band peak for armchair-type GNRs observed at 1604 and 1329 cm^{-1} , respectively (Fig. 3d), which is consistent with those of GNRs obtained by bottom-up synthesis⁴⁸. Double formants at 2649 , 2934 , and 3206 cm^{-1} were initially assigned to 2D, D + D', and 2D' peaks, respectively. The D-band peak can be explained by collective modes of the confined hexagonal rings for the confinement of π -electrons into a finite-size domain in large π -extended PAHs⁴⁹.

Solid-state ^{13}C NMR spectra were performed to confirm the structural changes before and after the Scholl reaction (Fig. S4). The characteristic single peak ($\delta = 31.28 \text{ ppm}$ for **P1** and 31.92 ppm for N-CNS) can be assigned to *t*-butyl carbons. **P1** shows multiple peaks ($\delta = 109.13$ – 162.02 ppm), which can be assigned to the aromatic carbons. The main aromatic ^{13}C NMR signals of N-CNS centered at -124 ppm , probably caused by main π -conjugated carbon atoms in the N-CNS. Moreover, the peaks of N-CNS in the aromatic zone move slightly to the lower field because of the increasing π -conjugation.

Physical properties

The photophysical properties of N-CNS and **P1** were characterized in solution by steady-state spectroscopy and time-resolved spectroscopy (Fig. 4). The absorption spectrum of **P1** only shows a narrow absorption band at 250 – 380 nm maximized at 300 nm . In sharp contrast, the UV-Vis spectrum of N-CNS in DMF showed a broad redshifted absorption band in the range of 260 – 800 nm maximized at $\sim 500 \text{ nm}$, indicating that a large π -conjugated structure was formed after cyclodehydrogenation. Furthermore, under an excitation at 350 nm , N-CNS exhibits a broad emission band at 440 – 820 nm maximized at 564 and 661 nm , demonstrating significant redshift compared to the reference precursor **P1** (maximized at 413 nm). This emission redshift is consistent with the UV-Vis result, indicating a large and well-extended conjugation nature in N-CNS. As shown in Fig. 4b, the precursor **P1** is a light-yellow solid, while N-CNS becomes a black solid. For comparison, the dilute DMF solution of N-CNS showed an intense red photoluminescence under irradiation by a hand-held UV lamp at $\lambda = 365 \text{ nm}$, while the precursor **P1** in solution presented an intense blue photoluminescence.

Moreover, the luminescence lifetime (τ_s) of precursor N-CNS and **P1** were measured by time-resolved fluorescence decay using the time-resolved photoluminescence (TRPL) technique (Figs. 4c, d). The luminescence lifetime of N-CNS follows second-order kinetics with lifetimes of 6.12 and 2.13 ns at 661 nm when excited at $\sim 420 \text{ nm}$. For comparison, **P1** shows longer fluorescence lifetimes at 16.64 and

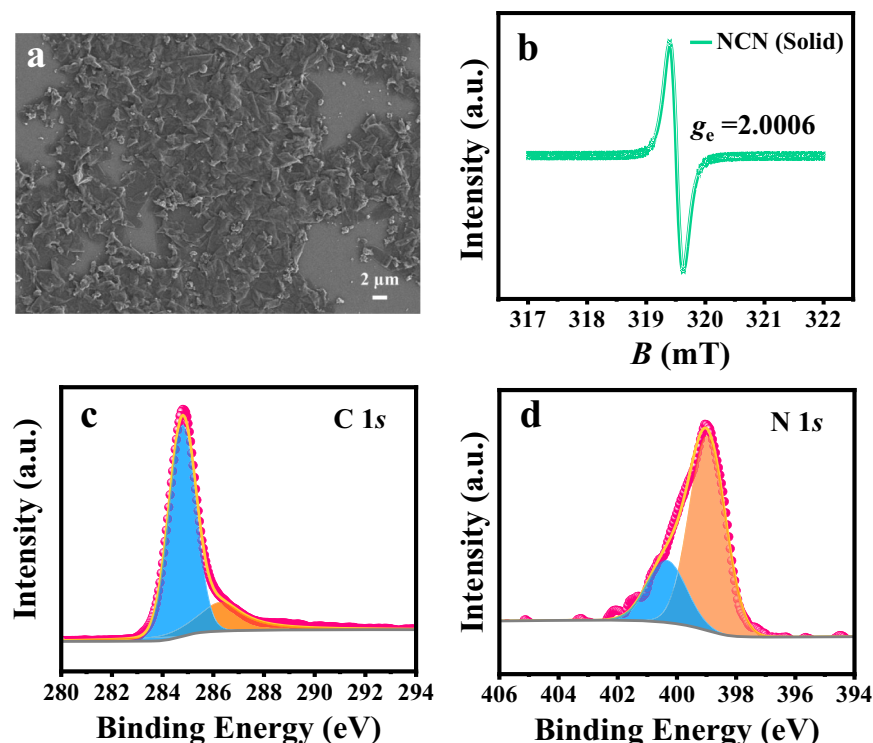


Fig. 5 | SEM, AFM, room temperature EPR spectrum and XPS spectra characterizations of N-CNS. **a** SEM image of bulk N-CNS, scale bar 4 μm ; inset, AFM image of N-CNS, scale bar 6 \AA . **b** Room temperature EPR spectrum of solid powder. **c** C 1s and **d** N 1s XPS spectra of N-CNS.

3.28 ns at 413 nm when excited at ~ 320 nm. The different emission lifetimes probably result from the different excited states of **PI** and **N-CNS**.

The morphology and microstructures of **N-CNS** were further investigated by scanning electron microscopy (SEM) and atomic force microscope (AFM). As shown in Fig. 5a, bulk **N-CNS** has layered structures consisting of thin sheets with micrometer-long wrinkles. AFM image showed that **N-CNS** can self-assemble into well-defined helix bundles on the surface (inset, Fig. 5a), which is consistent with our previous study.¹⁸ To further investigate the electronic properties of **N-CNS**, EPR measurements were carried out using a solid-state sample at room temperature (Fig. 5b). **N-CNS** displayed a typical single EPR peak, with a g_e value of -2.0006 , which confirms unpaired electrons and magnetic properties exist in this present solenoid material^{18,19}. Moreover, the chemical compositions and states of **N-CNS** were investigated by X-ray photoelectron spectroscopy (XPS). In Fig. 5c, C 1s spectrum of **N-CNS** shows two peaks at 284.8 and 286.3 eV, corresponding to sp^2 bonded carbon-carbon, and sp^2 bonded carbon-nitrogen ($\text{N}=\text{C}-\text{N}$), respectively. Figure 5d exhibits N 1s XPS spectra, the peak at 399.5 eV could correspond to sp^2 N bonding of ($\text{C}=\text{N}-\text{C}$). Ni 2p, Co 2p, Fe 2p, and Pd 3d XPS spectra of **N-CNS** are shown in Fig. S8. These results indicate that all metal elements involved in the synthetic reactions are absent from the samples, further demonstrating that **N-CNS** is a metal-free carbon material.

The explicit real-space structural elucidation of such organic molecules requires direct high-resolution structural imaging using electron microscopy. However, these strands of **N-CNS** organic molecules are extremely vulnerable to electron beam irradiation and thus prohibit traditional electron microscopy techniques from imaging the integral structures. The recent advances in low-dose electron microscopy allow the direct imaging of beam-sensitive materials⁵⁰⁻⁵², including metal-organic frameworks^{3,52-54}, covalent-organic framework^{52,55,56} and organic molecules⁵⁵. With the development of low-dose electron microscopy methods, integrated differential phase contrast scanning transmission electron microscopy (iDPC-STEM)

shows great advantages in the imaging of low-Z elements and electron beam-sensitive materials^{18,57,58}. Accordingly, we tried to image the organic **N-CNS** helices using the low-dose iDPC-STEM technique to maintain the structural integrity of these helices. Although the strands of **N-CNS** helices tend to bundle together due to the strong intermolecular interactions, prolonged probe sonication allows the segregation of a considerable fraction of single-strand **N-CNS** helices that can be clearly identified and elucidated by low-dose iDPC-STEM imaging. As we can see in Fig. 6, the intrinsic single-strand molecular structures of **N-CNS** helices can be clearly resolved from both [100] and [201] projections of the proposed 1D periodic structural model (Fig. S5). Figure 6a shows the iDPC-STEM image of a single-strand **N-CNS** helix projected along [100] axis, which exhibits fringe contrast characteristics for the periodic helical structures. The measured fringe spacing (b') of the **N-CNS** helix is 0.40 ± 0.03 nm and the helical width (d') is 2.4 ± 0.2 nm, respectively, which matches well with the proposed molecular structural model of **N-CNS** helix. As shown in Figs. 6c and S7, the calculated helical width of d is 25.12 \AA (without the consideration of *tert*-butyl) and the fringe spacing of b is 4.110 \AA ; then the resulting angle γ is 2.974° ($\gamma = \arctan(b/(d*\pi))$). It has been widely acknowledged that the iDPC-STEM contrast closely resembles the electrostatic potential of the chemical structure^{18,59}. The present results demonstrate the iDPC-STEM image contrast closely resembles the simulated projected potential map of the proposed **N-CNS** helix model, as shown in Figs. 6b and c. Moreover, the helical structural model is further validated from another iDPC-STEM image taken along the [201] direction of the structural model (Fig. 6d), from which the **N-CNS** helix is tilted away from the image plane as shown in Fig. 6f. The STEM image exhibits arrays of bright dots that corresponding to the projected columns of benzene rings in the **N-CNS** helix, which match well with the simulated projected potential map as shown in Fig. 6e. Taken together, low-dose iDPC-STEM imaging along both flat-lying and tilted projections of single-strand **N-CNS** helices unambiguously confirms the proposed molecular structural mode of nitrogen-doped carbon nanosolenoid with Riemann Surfaces.

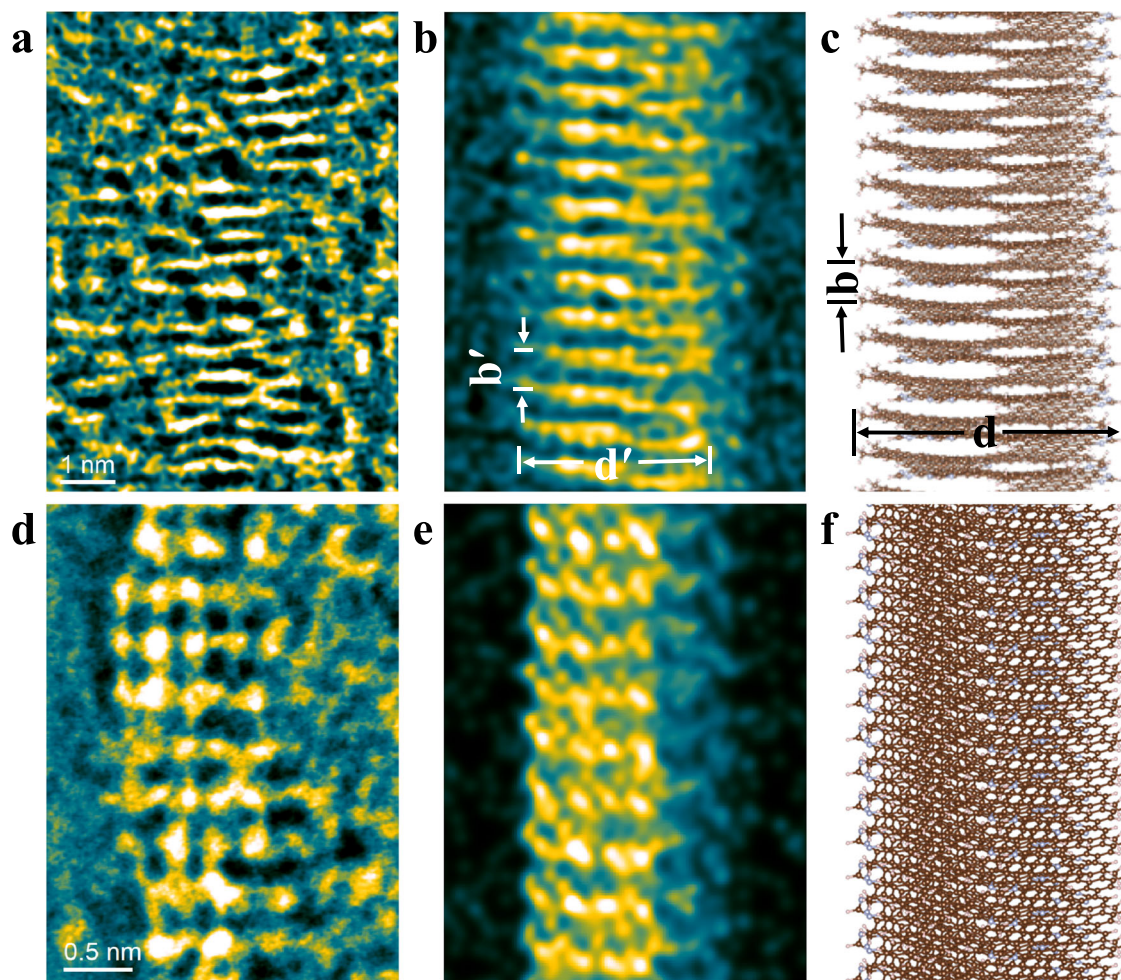


Fig. 6 | iDPC-STEM characterizations of N-CNS. Low-dose iDPC-STEM images (a, d), simulated projected potentials (b, e), and structural models (c, f) of single-strand N-CNS along [100] (upper figures) and [201] (lower figures) axes respectively. The false-colored images are rendered in aquatic color code. The structural

model used for simulating the electrostatic potential is constructed by adhering the single-strand N-CNS along a specific projection with a properly situated amorphous carbon layer with a thickness of 1 nm. A specific point-spread-function (PSF) width of 1.6 Å was used for the simulation.

Photocatalytic properties

Since N-CNS has excellent photophysical properties, it could be a potential metal-free photocatalyst for energy conversion. The photocatalytic H₂ evolution performance using N-CNS was further evaluated under the light irradiation of a 300 W Xe lamp equipped with a UV cut-off filter ($\lambda > 420$ nm). The typical photocatalytic H₂ production of N-CNS is schematically illustrated in Fig. 7a. Impressively, N-CNS can be used as a metal-free photocatalyst for hydrogen production in water. Figure 7b shows the photocatalytic activity of N-CNS for H₂ production in the presence of electron donors. With increasing concentrations of the electron donors (Na₂S and Na₂SO₃), the photocatalytic H₂ evolution rate rapidly increased and reached a maximum value of $190.2 \pm 21.2 \mu\text{mol g}^{-1} \text{h}^{-1}$ in the presence of 0.75 M Na₂S and 1.05 M Na₂SO₃. When the concentrations of Na₂S and Na₂SO₃ increased to 1.0 and 1.4 M, respectively, the H₂ evolution rate decreased to $182.8 \pm 17.5 \mu\text{mol g}^{-1} \text{h}^{-1}$, which is probably due to the loss of visible light energy hindered by the undissolved Na₂SO₃. Compared to N-CNS, the H₂ evolution rate of commercial photocatalyst TiO₂ P25 was only $5.5 \mu\text{mol g}^{-1} \text{h}^{-1}$ under the same conditions upon visible light irradiation (Table S2), indicating that N-CNS has better photocatalytic activity than P25 under visible light using the same reaction conditions. We also compared N-CNS with other metal-free materials reported in the literature for hydrogen evolution and these results are shown in Table S3. Most of these materials exhibited low H₂ evolution rates, and

only a few materials demonstrated rates higher than $100 \mu\text{mol g}^{-1} \text{h}^{-1}$. In contrast, the hydrogen evolution rate of N-CNS is $190 \mu\text{mol g}^{-1} \text{h}^{-1}$. This result demonstrated that N-CNS has good photocatalytic properties for H₂ production. Besides, the photocatalytic activity of N-CNS using different sacrificial electron donors was also measured for comparison (Fig. S9). As shown in Fig. 7d, the N-CNS photocatalyst exhibited excellent stability and maintained a similar photocatalytic activity for 36 h. An obvious transient photocurrent response was observed, suggesting the good photo-induced electron separation/transport property of N-CNS (Fig. S13). To confirm the electronic band positions of the as-prepared materials, Mott-Schottky (MS) measurements were carried out (Fig. S11). The conduction-band position is -0.46 eV (vs. NHE) for N-CNS. The absorption edge of N-CNS is located at 670 nm, corresponding to the band gap of 1.85 eV (Fig. S12). Combined with the band gap of N-CNS, the valence-band position can be determined as 1.39 eV (vs. NHE). All these results demonstrate that N-CNS can perform as a good metal-free photocatalyst for visible-light-driven H₂ evolution.

N-CNS can also be proposed as a novel photocatalyst to realize the C–H functionalization of 2-phenyl-1,2,3,4-tetrahydroisoquinoline (**1a**)^{60–63}. Catalytic activity of N-CNS toward photocatalytic aza-Henry reaction was further evaluated with **1a** and nitromethane as starting materials. The reaction was carried out in the presence of O₂ with a 9 W blue LED as the light source. To our delight, the desired C–H

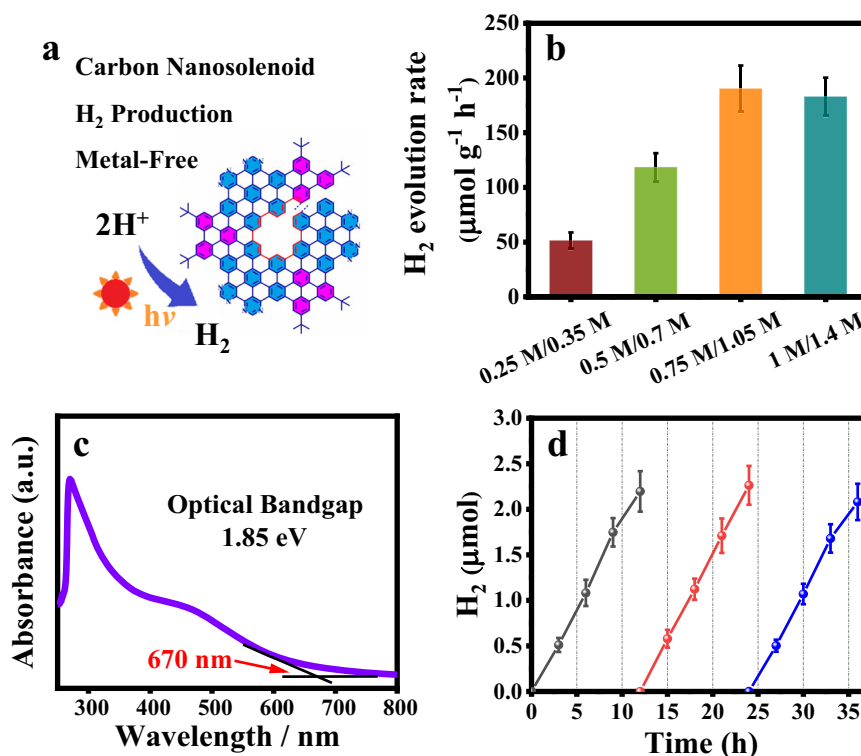


Fig. 7 | Photocatalytic H₂ production by N-CNS. **a** Schematic illustration of photocatalytic H₂ production by N-CNS. **b** H₂ evolution rate of N-CNS photocatalyst at different concentrations of the hole scavenger under visible light (wine: 0.25 M Na₂S and 0.35 M Na₂SO₃; green: 0.5 M Na₂S and 0.7 M Na₂SO₃; orange: 0.75 M Na₂S and 1.05 M Na₂SO₃; cyan: 1 M Na₂S and 1.4 M Na₂SO₃). **c** UV-Vis absorption

spectrum of N-CNS in DMF with calculated optical bandgap. **d** Cycling runs of N-CNS for photocatalytic H₂ evolution in the presence of 1.0 mg N-CNS photocatalyst in a 30 mL aqueous solution containing 0.75 M Na₂S and 1.05 M Na₂SO₃ (black: cycle 1; red: cycle 2; blue: cycle 3). The error bars in **b** and **d** show standard deviation (SD).

functionalization product **1b** was isolated in an excellent 95% yield by irradiation for 5 h with a catalytic amount of N-CNS (Table 1). And the use of visible light (300 W Xe lamp equipped with a UV cut-off filter, $\lambda > 420$ nm) resulted in a 90% yield. In sharp contrast, only a 9% yield of **1b** was obtained when the reaction was performed using the precursor **P1**. Control experiments revealed that catalyst, light, and oxygen are crucial for the formation of **1b**. Moreover, we also performed the absorption spectrum to investigate the stability of N-CNS before and after the photocatalytic aza-Henry reaction (Fig. S14). After the reaction, a three-step procedure including centrifugation, separation, and washing was done and N-CNS was performed in a new cycle, no significant loss of photocatalytic activity was observed after 10 cycles of 12 h (Fig. S22).

Besides the easy functionalization of tetrahydroisoquinoline, various other substituents were also subjected to photocatalytic organic transformations using N-CNS as the photocatalyst. As shown in Table 2, the catalytic results are also excellent for the benzylamine homocoupling reaction and oxygenation reaction of thioanisoles with all the yields >90%. Under light irradiation, the benzylamine homocoupling produced the product of N-benzyl-1-phenylmethanimine (**3a**) in a yield of 90.1%, as checked by ¹H NMR. Oxygenation reaction of methyl(phenyl)sulfane was performed under similar photocatalytic reaction conditions and the product of (methylsulfinyl)benzene (**3b**) had a yield as high as 94.9% in only 5 h. In addition, more sulfinylbenzene compounds with the amendment of different groups at the *para*-position, such as -OMe (**2c**), -F (**2d**), were examined. The yields of 1-methoxy-4-(methylsulfinyl)benzene (**3c**) and 1-fluoro-4-(methylsulfinyl)benzene (**3d**) were calculated to be 90.0% and 90.9%, respectively. All the high yields indicated that the N-CNS is an excellent metal-free photocatalyst in many photo-redox reactions.

Discussion

In summary, we reported a facile bottom-up synthesis of a large well-extended nitrogen-doped carbon nanosolenoid (N-CNS) with Riemann surface by a Pd-mediated Suzuki–Miyaura coupling followed by a Scholl reaction for cyclodehydrogenation. N-CNS was fully characterized by GPC, FTIR, Raman, solid-state ¹³C NMR spectra, and iDPC-STEM techniques. Its unique photophysical properties were investigated using UV-Vis, fluorescence, TRPL spectroscopy. Notably, N-CNS can be used as a simple polymeric metal-free photocatalyst for hydrogen production in water and a highly efficient photocatalyst such as aza-Henry reactions and oxygenation reactions of thioanisoles in the absence of any noble metals. The present results can shed light on the synthesis of novel carbon nanomaterials and explore their applications in solar energy conversion.

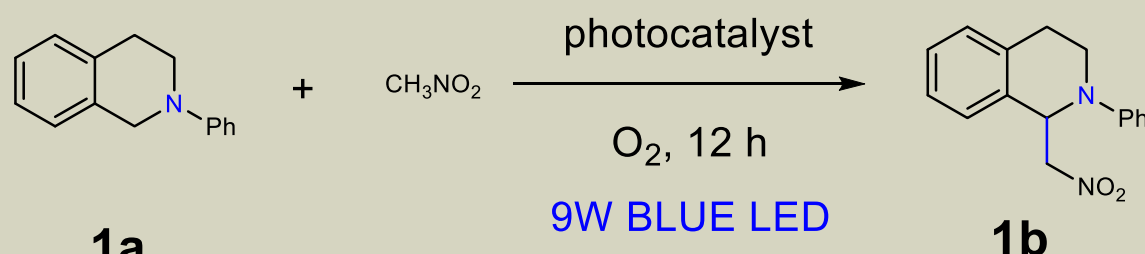
Methods

Compounds preparation

See Supplementary Information for details of the syntheses and characterization of **M1** and **M2**.

Synthesis of P1

To a degassed suspension of 5,5'-(6,11-dibromo-1,4-diphenyl-triphenylene-2,3-diyl)dipyrimidine (**M1**) (234 mg, 0.336 mmol), 2,2'-(4,4'-di-*tert*-butyl-[1,1':2',1''-terphenyl]-4',5'-diyl)bis(4,4,5,5-tetra-methyl-1,3,2-dioxaborolane) (**M2**) (200 mg, 0.336 mmol), potassium carbonate (465 mg, 3.36 mmol), Aliquat 336 (7.0 mg, 0.017 mmol, 5 mol%) in toluene (5 mL) and H₂O (1 mL) was added Pd(PPh₃)₄ (39.3 mg, 0.034 mmol), then the mixture was degassed for 15 min. The mixture was then heated at 110 °C for 60 h under a nitrogen atmosphere. Upon the reaction cooling to room temperature, the mixture was diluted with 1 M aqueous hydrochloric acid, extracted with CH₂Cl₂,

Table 1 | The photocatalytic aza-Henry reactions^a


Variation	Yield of 1b (%) ^b
No photocatalyst	Trace
No light	Trace
No O ₂	22.2
P1	9.1
N-CNS with visible light	90.0
N-CNS	95.1

^aReaction conditions: 2-phenyl-1,2,3,4-tetrahydroisoquinoline **1a** (0.5 mmol), photocatalyst (1.5 mg), CH₃NO₂ (3 mL), O₂ (1 atm), LED lamp (9 W).

^bIsolated yield.

and concentrated under vacuum. The resulting precipitate was washed intensively with 0.5 M HCl solution in water, filtered, and washed with water, methanol, acetone, methanol, and hexane. The precipitate was collected, giving 304 mg of polymer **P1** as a pale yellow solid (yield: 83%).

Synthesis of N-CNS

After a solution of polymer **P1** (500 mg, 0.55 mmol), 2,3-dichloro-5,6-dicyanobenzoquinone (DDQ: 2.01 g, 8.9 mmol) in anhydrous DCM (50 mL) was degassed with argon for 20 min, trifluoromethanesulfonic acid (3.0 mL) was added to the mixture. Then the reaction mixture was stirred at 0 °C for another 24 h under an argon atmosphere and quenched with saturated NaHCO₃ solution, filtered, and washed with methanol, acetone, CH₂Cl₂, and methanol. The precipitate was collected to obtain the title polymer **N-CNS** as a dark black solid (yield: 76%); $M_n = 65,391 \text{ g mol}^{-1}$ and $M_w = 149,204 \text{ g mol}^{-1}$ by GPC.

Aza-Henry reaction

To a flame-dried 10 mL vial equipped with a magnetic stir bar with **1a** (104.6 mg, 0.5 mmol) and **N-CNS** (1.5 mg). Nitromethane solvent (3 mL) was transferred to the vial via syringe under oxygen and stirred at a blue LED lamp (9 W) for 5 h. After the reaction, the **N-CNS** was separated by centrifugation and washed with DCM which could be used for the catalyzer again. The crude product **1b** was in the solvent and purified by silica gel chromatography to afford the desired **1b** as a yellow oil in a yield of 95% (127.5 mg). ¹H NMR (CDCl₃, 400 MHz): δ 7.33–7.16 (m, 5H), 7.13 (d, *J* = 7.2 Hz, 1H), 6.98 (d, *J* = 8.2 Hz, 2H), 6.85 (t, *J* = 7.3 Hz, 1H), 5.55 (t, *J* = 7.2 Hz, 1H), 4.87 (dd, *J* = 11.8, 7.8 Hz, 1H), 4.56 (dd, *J* = 11.8, 6.6 Hz, 1H), 3.71–3.56 (m, 2H), 3.14–3.04 (m, 1H), 2.84–2.75 (m, 1H).

The recycling process of **N-CNS** photocatalytic for aza-Henry reaction: To a flame-dried 10 mL vial equipped with a magnetic stir bar with **1a** (104.6 mg, 0.5 mmol) and recycling **N-CNS** (1.5 mg). Nitromethane as the solvent (3 mL) was transferred into the vial via syringe under oxygen and stirred under a blue LED lamp (9 W) for 5 h. Then, the **N-CNS** catalyst was recovered for another cycle. After a few new cycles, the product **1b** can be still obtained with a similar yield.

Benzylamine homocoupling reaction

To a flame-dried 10 mL vial equipped with a magnetic stir bar with **2a** (1 mmol) and **N-CNS** (1.5 mg). MeCN (3 mL) was transferred to the vial

via syringe under oxygen and stirred at a blue LED lamp (9 W) for 5 h. The mixture was filtered to remove the catalyst to get main product **3a**. The yields were determined by ¹H NMR analysis (Fig. S18).

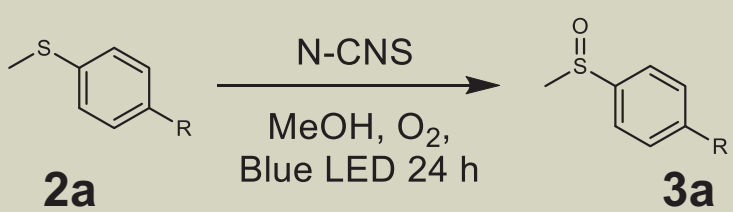
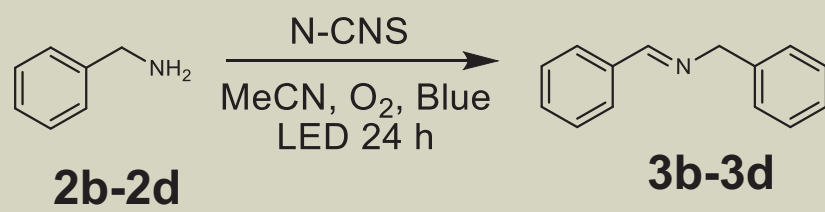
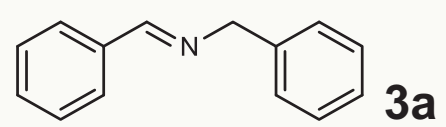
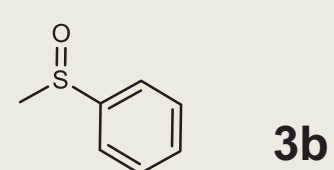
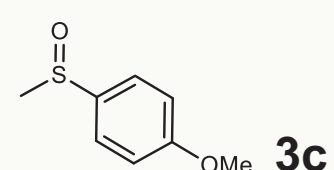
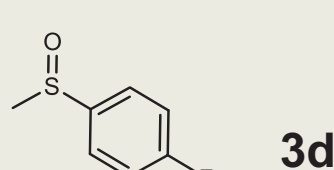
Photocatalytic oxidation of thioethers

To a flame-dried 10 mL vial equipped with a magnetic stir bar with **2b–2d** (1 mmol) and **N-CNS** (1.5 mg). MeOH (3 mL) was transferred to the vial via syringe under oxygen and stirred at a blue LED lamp (9 W) for 5 h. The mixture was filtered to remove the catalyst to get the main product **3b–3d**. The yields were determined by ¹H NMR analysis (Figs. S19–S21).

Spectroscopic analysis

High-resolution mass spectrometry (HR-MS) analyses were carried out using MALDI-TOF-MS techniques. NMR spectra were recorded on Bruker BioSpin (¹H 400 MHz, ¹³C 100 MHz) spectrometer, and chemical shifts were reported as the delta scale in ppm relative to CDCl₃ (δ = 7.26 ppm) for ¹H NMR and CDCl₃ (δ = 77.0 ppm) for ¹³C NMR. Data are reported as follows: chemical shift, multiplicity (s = singlet, d = doublet, t = triplet, m = multiplet, br = broad signal), coupling constant (Hz), and integration. UV-vis absorption spectra were performed on a UNIC-3802 spectrophotometer. Atomic force microscope (AFM) measurements were performed using a Dimension ICON microscope (Bruker) in the tapping mode in a clean room environment. All anhydrous solvents and starting chemical reagents for syntheses were purchased from commercial suppliers (Aldrich or Acros) and used without further purification unless otherwise noted. All moisture- or air-sensitive reactions were carried out in a dry reaction vessel under an inert atmosphere (argon or nitrogen) using standard Schlenk techniques. Preparative column chromatography was performed on silica gel (size 200–300 mesh). Analytical thin-layer chromatographies (TLC) were performed with silica gel HSGF 254. Flash chromatography was performed on silica gel (300–400 mesh). Gel permeation chromatography (GPC) was carried out using a G1316A PL gel column with a rate of 1.0 min/mL in DMF assured by G1310B Iso.pump and detected by a G1362A differential refractive index detector. The solid-state ¹³C NMR experiments were conducted on a Bruker AVANCE NEO600WB spectrometer (¹H 600.16 MHz, ¹³C 150.93 MHz) using a Bruker 3.2 mm H/X/Y probe. The samples were packed in 3.2 mm o.d. ZrO₂ rotos. Gly was used as an external reference to calibrate the

Table 2 | The photocatalytic oxygenation of benzylamine and thioanisoles^a

 <p>2a 3a</p>	 <p>2b-2d 3b-3d</p>
Product	Yields (%)^b
 <p>3a</p>	90.1
 <p>3b</p>	94.9
 <p>3c</p>	90.0
 <p>3d</p>	90.9

^aReaction conditions: benzylamine **2a** (0.5 mmol), photocatalyst (1.5 mg), MeCN (3 mL), O₂ (1 atm), blue LED lamp (9 W); thioanisole **2b–2d** (0.5 mmol), photocatalyst (1.5 mg), MeOH (3 mL), O₂ (1 atm), blue LED lamp (9 W).

^bThe yields were determined by ¹H NMR.

radiofrequency (rf) field strength and chemical shift scale (δ (¹³C) = 176.03 ppm).

The iDPC-STEM imaging

The low-dose high-resolution iDPC-STEM images were obtained under a Cs-corrected electron microscope operated at 300 kV. The beam current was reduced to 1 pA, the convergence angle was 25 mrad and the collection angle of iDPC-STEM imaging was set to 7–29 mrad. The projected electrostatic potential was simulated using the QSTEM code with a point-spread-function (PSF) width of 1.5 Å over a single-strand CNS structural model embedded in a 1 nm-thick amorphous carbon layer.

Computational details

Geometrical structure and electronic structures of N-CNS. Geometrical optimization of the whole cell was carried out utilizing the Vienna an initio simulation package (version: VASP 6.3.1)⁶⁴. Perdew–Burke–Ernzerhof (PBE)⁶⁵ in terms of the gradient of electronic density described the exchange and correlation (XC) interaction in the Kohn–Sham equation. The interaction between ions and electrons was treated by the projector-augmented wave (PAW)⁶⁶-based pseudopotential, featuring greater computational efficiency as well as high accuracy. Specifically, outer electrons of C, H, and N atoms were explicitly treated as valence electrons. Plane-wave function with kinetic

energy less than the energy of 450 eV is included in the basic set. The $1 \times 1 \times 16$ k -point grids based on the strategy of Monkhorst–Pack⁶⁷, featuring enough accuracy in the calculation of total energy via convergence test, were used to sample in the Brillouin zone. During the calculations, the convergence value was set to 1.0×10^{-5} eV for self-consistent field calculations, and the geometrical optimization will keep running until <0.02 eV/Å of Hellmann–Feynman force per atom.

Photocatalytic experiments

The photocatalytic H₂ evolution experiments were carried out in a 50 mL flask with stirring at room temperature using a 300 W Xe lamp equipped with a UV cut-off filter ($\lambda > 420$ nm). 2.0 mg of the photocatalyst was dispersed in 30 mL of aqueous solution containing 6 mL DMF for dissolution of **N-CNS** and Na₂S and Na₂SO₃ as sacrificial reagents. Before irradiation, the solution was bubbled with high-purity nitrogen for 20 min to remove the air.

Photoelectrochemical measurements

Photoelectrochemical measurements were carried out on a CHI 660e electrochemical workstation in a standard three-electrode electrochemical cell with the photocatalyst-coated FTO as the working electrode, a platinum wire as a counter electrode, and a saturated Ag/AgCl electrode as a reference electrode. A sodium sulfate solution (0.2 M Na₂SO₄) was used as the electrolyte. 1 mg **N-CNS** powder was mixed with 1.0 mL acetonitrile and 50 μ L Nafion and sonicated for 10 min. The working electrodes were prepared by dropping the suspension (50 μ L) evenly onto the surface of the FTO plates and dried at room temperature. The Mott–Schottky plots were measured at the frequencies of 1500, 2000, and 2500 Hz.

Data availability

Materials and methods, experimental procedures, useful information, characterization studies, ¹H NMR spectra, ¹³C NMR spectra, and mass spectrometry data are available in the Supplementary Information. Additional data that support the findings of this study are available from the corresponding author upon request.

References

- Baldridge, K. K. & Siegel, J. S. Of graphs and graphenes: Molecular design and chemical studies of aromatic compounds. *Angew. Chem. Int. Ed.* **52**, 5436–5438 (2013).
- Pun, S. H. et al. Synthesis, structures, and properties of hepta-benzo[7]circulene and octabenz[8]circulene. *J. Am. Chem. Soc.* **141**, 9680–9686 (2019).
- Zhang, Y. Q. et al. Charging a negatively curved nanographene and its covalent network. *J. Am. Chem. Soc.* **143**, 5231–5238 (2021).
- Cheung, K. Y., Chan, C. K., Liu, Z. F. & Miao, Q. A twisted nanographene consisting of 96 carbon atoms. *Angew. Chem. Int. Ed.* **56**, 9003–9007 (2017).
- Daigle, M., Miao, D., Lucotti, A., Tommasini, M. & Morin, J. F. Helically coiled graphene nanoribbons. *Angew. Chem. Int. Ed.* **56**, 6213–6217 (2017).
- Mehta, G. & Sarma, P. V. S. A rapid, two step construction of novel C₄₈H₂₄ and C₅₄H₂₄ polycyclic aromatic hydrocarbons represented on the C₆₀-fullerene surface via a threefold intramolecular heck coupling reaction. *Tetrahedron Lett.* **43**, 6557–6560 (2002).
- Chen, M. Q. et al. Anomalous cis-conformation regioselectivity of heterocycle-fused Sc₃N@D₃h-C₇₈ derivatives. *Angew. Chem. Int. Ed.* **60**, 7880–7886 (2021).
- Ayalon, A. et al. Stable high-order molecular sandwiches: hydrocarbon polyanion pairs with multiple lithium ions inside and out. *Science* **265**, 1065–1067 (1994).
- Scott, L. T. et al. A rational chemical synthesis of C₆₀. *Science* **295**, 1500–1503 (2002).
- Iijima, S. Helical microtubules of graphitic carbon. *Nature* **354**, 56–58 (1991).
- Liu, B. L., Wu, F. Q., Gui, H., Zheng, M. & Zhou, C. W. Chirality-controlled synthesis and applications of single-wall carbon nanotubes. *ACS Nano* **11**, 31–53 (2017).
- Nakakuki, Y., Hirose, T., Sotome, H., Miyasaka, H. & Matsuda, K. Hexa-peri-hexabenz[7]helicene: homogeneously π -extended helicene as a primary substructure of helically twisted chiral graphenes. *J. Am. Chem. Soc.* **140**, 4317–4326 (2018).
- Chen, Y. et al. Double π -extended undecabenz[7]helicene. *Angew. Chem. Int. Ed.* **60**, 7796–7801 (2021).
- Ma, S. et al. Supertwistacene: a helical graphene nanoribbon. *J. Am. Chem. Soc.* **142**, 16887–16893 (2020).
- Zhu, Y. P., Guo, X. Y., Li, Y. & Wang, J. B. Fusing of seven HBCs toward a green nanographene propeller. *J. Am. Chem. Soc.* **141**, 5511–5517 (2019).
- Beser, U. et al. A C₂₁₆-nanographene molecule with defined cavity as extended coronoid. *J. Am. Chem. Soc.* **138**, 4322–4325 (2016).
- Robertson, A. W. et al. Atomic structure of graphene subnanometer pores. *ACS Nano* **9**, 11599–11607 (2015).
- Wang, J. Y. et al. Synthesis of a magnetic π -extended carbon nanosolenoid with Riemann surfaces. *Nat. Commun.* **13**, 1239 (2022).
- Xu, F. B., Yu, H., Sadrzadeh, A. & Yakobson, B. I. Riemann surfaces of carbon as graphene nanosolenoids. *Nano Lett.* **16**, 34–39 (2016).
- Lenosky, T., Gonze, X., Teter, M. & Elser, V. Energetics of negatively curved graphitic carbon. *Nature* **355**, 333–335 (1992).
- Odkhuu, D. et al. Negatively curved carbon as the anode for lithium ion batteries. *Carbon* **66**, 39–47 (2014).
- Li, X. L., Wang, X. R., Zhang, L., Lee, S. W. & Dai, H. J. Chemically derived, ultrasoft graphene nanoribbon semiconductors. *Science* **319**, 1229–1232 (2008).
- Ritter, K. A. & Lyding, J. W. The influence of edge structure on the electronic properties of graphene quantum dots and nanoribbons. *Nat. Mater.* **8**, 235–242 (2009).
- Son, Y. W., Cohen, M. L. & Louie, S. G. Half-metallic graphene nanoribbons. *Nature* **444**, 347–349 (2006).
- Cai, J. M. et al. Atomically precise bottom-up fabrication of graphene nanoribbons. *Nature* **466**, 470–473 (2010).
- Narita, A. et al. Synthesis of structurally well-defined and liquid-phase-processable graphene nanoribbons. *Nat. Chem.* **6**, 126–132 (2014).
- Narita, A., Wang, X. Y., Feng, X. L. & Müllen, K. New Advances in nanographene chemistry. *Chem. Soc. Rev.* **44**, 6616–6643 (2015).
- Bronner, C. et al. Aligning the band gap of graphene nanoribbons by monomer doping. *Angew. Chem. Int. Ed.* **52**, 4422–4425 (2013).
- Trauzettel, B., Bulaev, D. V., Loss, D. & Burkard, G. Spin qubits in graphene quantum dots. *Nat. Phys.* **3**, 192–196 (2007).
- Zhang, Y. et al. Direct visualization of atomically precise nitrogen-doped graphene nanoribbons. *Appl. Phys. Lett.* **105**, 023101 (2014).
- Nguyen, G. D. et al. Bottom-up synthesis of $N=13$ sulfur-doped graphene nanoribbons. *J. Phys. Chem. C* **120**, 2684–2687 (2016).
- Błoński, P. et al. Doping with graphitic nitrogen triggers ferromagnetism in graphene. *J. Am. Chem. Soc.* **139**, 3171–3180 (2017).
- Babar, R. & Kabir, M. Ferromagnetism in nitrogen-doped graphene. *Phys. Rev. B: Condens. Matter Mater. Phys.* **99**, 115442 (2019).
- Zheng, X. H., Wang, X. L., Abtew, T. A. & Zeng, Z. Building half-metallicity in graphene nanoribbons by direct control over edge states occupation. *J. Phys. Chem. C* **114**, 4190–4193 (2010).
- Li, Y. F., Zhou, Z., Shen, P. W. & Chen, Z. F. Spin gapless semiconductor-metal-half-metal properties in nitrogen-doped zig-zag graphene nanoribbons. *ACS Nano* **3**, 1952–1958 (2009).
- Cai, J. M. et al. Graphene nanoribbon heterojunctions. *Nat. Nanotechnol.* **9**, 896–900 (2014).

37. Pawlak, R. et al. Bottom-up synthesis of nitrogen-doped porous graphene nanoribbons. *J. Am. Chem. Soc.* **142**, 12568–12573 (2020).
38. Sharma, S. & Basu, S. Fabrication of centimeter-sized $\text{Sb}_2\text{S}_3/\text{SiO}_2$ monolithic *Mimosa pudica* nanoflowers for remediation of hazardous pollutants from industrial wastewater. *J. Clean. Prod.* **280**, 124525 (2021).
39. Sharma, S. & Basu, S. Visible-light-induced photocatalytic response of easily recoverable $\text{Mn}_2\text{O}_3/\text{SiO}_2$ monolith in centimeter-scale towards degradation of ofloxacin: performance evaluation and product analysis. *Chemosphere* **307**, 135973 (2022).
40. Winant, P. & Dehaen, W. A visible-light-induced, metal-free bis-arylation of 2,5-dichlorobenzoquinone. *W. Beilstein J. Org. Chem.* **17**, 2315–2320 (2021).
41. Wu, Q. Y. et al. A function-switchable metal-free photocatalyst for the efficient and selective production of hydrogen and hydrogen peroxide. *J. Mater. Chem. A* **8**, 11773–11780 (2020).
42. Zhu, M. et al. Metal-free photocatalyst for H_2 evolution in visible to near-infrared region: Black phosphorus/graphitic carbon nitride. *J. Am. Chem. Soc.* **139**, 13234–13242 (2017).
43. Fang, Y. X. & Wang, X. C. Metal-free boron-containing heterogeneous catalysts. *Angew. Chem. Int. Ed.* **56**, 15506–15518 (2017).
44. Liu, X. & Dai, L. M. Carbon-based metal-free catalysts. *Nat. Rev. Mater.* **1**, 16064 (2016).
45. Centrone, A. et al. Structure of new carbonaceous materials: the role of vibrational spectroscopy. *Carbon* **43**, 1593–1609 (2005).
46. Wu, J. S. et al. From branched polyphenylenes to graphite ribbons. *Macromolecules* **36**, 7082–7089 (2003).
47. Schwab, M. G. et al. Structurally defined graphene nanoribbons with high lateral extension. *J. Am. Chem. Soc.* **134**, 18169–18172 (2012).
48. Negri, F., Castiglioni, C., Tommasini, M. & Zerbi, G. A computational study of the Raman spectra of large polycyclic aromatic hydrocarbons: toward molecularly defined subunits of graphite. *J. Phys. Chem. A* **106**, 3306–3317 (2002).
49. Castiglioni, C., Tommasini, M. & Zerbi, G. Raman spectroscopy of polyconjugated molecules and materials: confinement effect in one and two dimensions. *Philos. Trans. A Math. Phys. Eng. Sci.* **362**, 2425–2459 (2004).
50. Chen, Q. et al. Imaging beam-sensitive materials by electron microscopy. *Adv. Mater.* **32**, 1907619–1907661 (2020).
51. Zhang, D. et al. Atomic-resolution transmission electron microscopy of electron beam-sensitive crystalline materials. *Science* **359**, 675–679 (2018).
52. Peng, Y. et al. Ultrathin two-dimensional covalent organic framework nanosheets: preparation and application in highly sensitive and selective DNA detection. *J. Am. Chem. Soc.* **139**, 8698–8704 (2017).
53. Xu, K. et al. On-surface synthesis of a nonplanar porous nanographene. *J. Am. Chem. Soc.* **141**, 7726–7730 (2019).
54. Li, X. et al. Direct imaging of tunable crystal surface structures of MOF MIL-101 using high-resolution electron microscopy. *J. Am. Chem. Soc.* **141**, 12021–12028 (2019).
55. Gong, C. T. et al. Synthesis and visualization of entangled 3D covalent organic frameworks with high-valency stereoscopic molecular nodes for gas separation. *Angew. Chem. Int. Ed.* **61**, e202204899 (2022).
56. Peng, Y. et al. Intramolecular hydrogen bonding-based topology regulation of two-dimensional covalent organic frameworks. *J. Am. Chem. Soc.* **142**, 13162–13169 (2020).
57. Shen, B. Y. et al. A single-molecule van der Waals compass. *Nature* **592**, 541–544 (2021).
58. Shen, B. Y. et al. Atomic imaging of zeolite-confined single molecules by electron microscopy. *Nature* **607**, 703–707 (2022).
59. Liu, L. M. et al. Direct imaging of atomically dispersed molybdenum that enables locating aluminum in the framework of zeolite ZSM-5. *Angew. Chem. Int. Ed.* **59**, 819–825 (2020).
60. Condie, A. G., González-Gómez, J. C. & Stephenson, C. R. J. Visible-light photoredox catalysis: Aza-Henry reactions via C–H functionalization. *J. Am. Chem. Soc.* **132**, 1464–1465 (2010).
61. Shi, L. & Xia, W. J. Photoredox functionalization of C–H bonds adjacent to a nitrogen atom. *Chem. Soc. Rev.* **41**, 7687–7697 (2012).
62. Wang, S. X. et al. Ligand modification of Au_{25} nanoclusters for near-infrared photocatalytic oxidative functionalization. *J. Am. Chem. Soc.* **144**, 3787–3792 (2022).
63. Xie, Z. G., Wang, C., deKrafft, K. E. & Lin, W. B. Highly stable and porous cross-linked polymers for efficient photocatalysis. *J. Am. Chem. Soc.* **133**, 2056–2059 (2011).
64. Kresse, G. & Furthmüller, J. Efficient iterative schemes for ab initio total-energy calculations using a plane-wave basis set. *J. Phys. Rev. B* **54**, 11169–11186 (1996).
65. Blöchl, P. E. Projector augmented-wave method. *Phys. Rev. B* **50**, 17953 (1994).
66. Perdew, J. P., Burke, K. & Ernzerhof, M. Generalized gradient approximation made simple. *Phys. Rev. Lett.* **77**, 3865–3868 (1996).
67. Monkhorst, H. J. & Pack, J. D. Special points for Brillouin-zone integrations. *Phys. Rev. B* **13**, 5188–5192 (1976).

Acknowledgements

This work was financially supported by the National Natural Science Foundation of China (22225108, 21971229, 52172053, 22075250, 22122505, 21771161) and the National Key Research and Development Program of China (2022YFE0113800).

Author contributions

P.D. conceived and designed this research with the help of M.C. and Y. Zhou; Y. Zhou and S.W. synthesized the **N-CNS** material and conducted all characterizations, and EPR measurements. G.S. and Y. Zhu acquired low-dose high-resolution iDPC-STEM images. G.Z. did all the calculation studies. Y. Zhou, M.C., X.Z., and S.W. carried out photophysical studies. Y. Zhou did FT-IR, ^{13}C NMR measurements, and photocatalytic reactions. Y. Zhou, M.C., S.W., X.Z., Y. Zhu, G.S., G.Z., and P.D. co-wrote the paper, and all the authors commented on it.

Competing interests

The authors declare no competing interests.

Additional information

Supplementary information The online version contains supplementary material available at <https://doi.org/10.1038/s41467-023-41467-4>.

Correspondence and requests for materials should be addressed to Muqing Chen, Yihan Zhu or Pingwu Du.

Peer review information *Nature Communications* thanks Soumen Basu, and the other, anonymous, reviewers for their contribution to the peer review of this work. A peer review file is available.

Reprints and permissions information is available at <http://www.nature.com/reprints>

Publisher's note Springer Nature remains neutral with regard to jurisdictional claims in published maps and institutional affiliations.

Open Access This article is licensed under a Creative Commons Attribution 4.0 International License, which permits use, sharing, adaptation, distribution and reproduction in any medium or format, as long as you give appropriate credit to the original author(s) and the source, provide a link to the Creative Commons licence, and indicate if changes were made. The images or other third party material in this article are included in the article's Creative Commons licence, unless indicated otherwise in a credit line to the material. If material is not included in the article's Creative Commons licence and your intended use is not permitted by statutory regulation or exceeds the permitted use, you will need to obtain permission directly from the copyright holder. To view a copy of this licence, visit <http://creativecommons.org/licenses/by/4.0/>.

© The Author(s) 2023